CrossMark

Open-pit mine geomorphic changes analysis using multi-temporal UAV survey

Jie Xiang[1] · Jianping Chen[1] · Giulia Sofia[2] · Yi Tian[3] · Paolo Tarolli[2]

Abstract

Mining activities, and especially open-pit mines, have a significant impact on the Earth's surface. They influence vegetation cover, soil properties, and hydrological conditions, both during mining and for many years after the mines have been deactivated. Exploring a fast, accurate, and low-cost method to monitor changes, through years, in such an anthropogenic environment is, therefore, an open challenge for the Earth Science community. We selected a case study located in the northeast of Beijing, to assess geomorphic changes related to mining activities. In 2014 and 2016, an unmanned aerial vehicle (UAV) collected two series of high-resolution images. Through the structure-from-motion photogrammetric technique, the images were used to generate high-resolution digital elevation models (DEMs). The assessment of geomorphic changes was carried out by two methodologies. At first, we quantitatively estimated the detectable area, volumetric changes, and the mined tonnage by using the DEM of difference (DoD), which calculated the differences between two DEMs on a cells-by-cells basis. Secondly, the slope local length of autocorrelation (SLLAC) allowed determining the surface covered by open-pit mining by using an empirical model extracting the extent of the open-pit. The analysis of the DoD allows estimating the areal changes and the volumetric changes. The analysis of the SLLAC and its derived parameter allows for the accurate depiction of terraces and the extent of changes within the open-pit mine. Our results underlined how UAVs equipped with high-resolution cameras can be fast, precise, and low-cost instruments for obtaining multi-temporal topographic information, especially when combined with suitable methodologies to analyze the surface geomorphology, for dynamic monitoring of open-pit mines.

Keywords UAV · DEM · SLLAC · DoD · Open-pit mine

Introduction

Anthropogenic landscapes cover a significant extent of the Earth's surface, to the point that the concept of Anthropocene has been widely discussed also in geomorphology (Brown et al. 2017; Lewin and Macklin 2014; Tarolli and Sofia 2016). In many of these landscapes, the impact of mining activities on the geomorphic system is significant (Chen et al. 2015; Ellis 2011; Sofia et al. 2014; Tarolli and Sofia 2016). In particular, open-pit mines can influence vegetation cover, soil properties, and hydrological conditions, by changing the surface hydrology, flow paths, and groundwater level (Osterkamp and Joseph 2000; Mossa and James 2013; Tarolli 2014). The most recent reviews (Mossa and James 2013; Tarolli and Sofia 2016) about mining summarized four main issues related to the impact of mining on geomorphic systems: erosion, subsidence, hazards, and runoff. It is not possible to overcome these critical impacts in short time, as they continue even years after mining activities stopped. Even when reclaimed, the landscape is left in a condition hydrologically more similar to urban areas, rather than a natural reclaimed landscape (Tarolli and Sofia 2016). Mining activities always accompany human development and progress. In recent years, the rapid urbanisation and industrialization are spurring a rising demand for building materials, base metals, and industrial minerals (Kobayashi et al. 2014), and this trend will not cease by 2050 according to the predictions (Vidal et al. 2013). Therefore, monitoring of open-pit mines in anthropogenic landscapes represents a

✉ Jianping Chen
3s@cugb.edu.cn

Extended author information available on the last page of the article

challenge for better supporting a sustainable environment planning.

The analysis of open-pit mines through geomorphology can improve the understanding of the mechanisms responsible for environmental effects, and help to find the most appropriate strategies for reclamation (Toy and Hadley 1987; Wilkinson and McElroy 2007). This monitoring requires a continuous assessment of the extent of the mine, of the surface topography, and a detection of surface changes that could be related to extraction activities. In the last decade, recent advances in ground-based, airborne-based, and remotely sensed surveying technologies, such as aerial and terrestrial light detection and ranging (LiDAR) and structure from motion (SfM), revolutionized the collection of topographic data. However, limitations arise when using some technologies for real-time or near-real-time monitoring of open-pit mines. Ground surveys are time-consuming and have sparse spatial coverage (Turner et al. 2015). Terrestrial laser scanners have problems with inhomogeneous point densities and data holes in shadowed areas (Haas et al. 2016). LiDAR high-resolution topographic surveying requires traditionally high capital and logistical costs. Also, the spatial resolution of the majority of existing active and passive remote sensors is typically too coarse to create digital elevation models (DEMs) for detailed geomorphological applications (Westoby et al. 2012).

In recent years, the low-cost photogrammetric method SfM ideally suited for low-budget research and applications emerged as a new efficient monitoring technology (Eltner et al. 2016; Westoby et al. 2012). Coupled with unmanned aerial vehicles (UAVs), and with the developments of autopilot systems, high-quality digital cameras and miniature GPS, it offers a perfect tool to collect ultra-high-resolution imagery (Colomina and Molina 2014; Lucieer et al. 2014; Turner et al. 2015). These advances make monitoring geomorphic changes through repeated topographic surveys and the application of morphological algorithms a tractable, affordable approach. By now, the scientific community, in general, provided different analyses on geomorphic changes using UAVs in various environment context (Jaakkola et al. 2010; Niethammer et al. 2012; Westoby et al. 2012; Colomina and Molina 2014; Immerzeel et al. 2014; Lucieer et al. 2014; Turner et al. 2015; Woodget et al. 2015; Francioni et al. 2015; Neugirg et al. 2016; Yucel and Turan 2016; Eltner et al. 2016; Fernández et al. 2016; Haas et al. 2016; Cook 2017). Haas et al. (2016) estimated the net change in storage for morphological sediment budgets; Immerzeel et al. (2014) monitored the Himalayan glacier dynamics; Turner et al. (2015) assessed landslide dynamics.

Although there are plenty of examples of UAVs and SfM technologies applications in geomorphology in the last few years, there are only a few publications related to their applicability in the monitoring of surface mining. McLeod et al.

(2013), Hugenholtz et al. (2015), Lee and Choi (2015), and Shahbazi et al. (2015) used UAVs to measure fracture orientation in open-pit mine, calculate the earthwork volume, analyze details of topography, and model the mines using 3D point clouds, respectively. Esposito et al. (2017) used UAV derived point clouds for multi-temporal estimation of the surface extent and volume changes in an open-pit mine in Sardinia. Francioni et al. (2015) and Tong et al. (2015) assessed the slope stability of an open-pit using a 3D finite difference method based on the 3D model derived by UAVs and TLS.

A further step, in term of open-pit mine analysis, was provided by Chen et al. (2015). That research proposed a useful framework to detect the extent of the open-pit, based on the landscape metric slope local length of autocorrelation (SLLAC, Sofia et al. 2014), and high-resolution topography derived by UAV and SfM. Haas et al. (2016) provided a quantification and analysis of geomorphic processes of a cultivated iron mine on the Italian island of Elba using photographs from TLS and UAV over a period of 5 years.

The purpose of this contribution, starting from the outcomes and future challenges suggested by Chen et al. (2015), is to establish a fast, accurate and low-cost workflow to assess the geomorphic changes through times. To this purpose, the method is based on multi-temporal high-resolution DEMs derived from UAV and SfM. This methodology could not only to support effective management of mining but also sustainable environmental planning.

Study area

The Miyun Iron Mine is located in the Juge Town (116°58′12″E, 40°22′46″N), approximately 80 km northeast of Beijing and about 6 km from the Miyun Reservoir, which is a primary source of drinking water in Beijing (Fig. 1) (Huang et al. 2013). The climatic conditions of the region are characterized by a mean annual rainfall of around 780 mm, with main precipitation occurring during the summer period and an average temperature of 10 °C. This area has a long history in iron extraction. The Miyun Mine was founded in 1959 and became operational in 1970. It spans from −40 to 240 m a.s.l., and it covers an area of about 17 km^2. This mine is one of the largest mines in Beijing district, reserving more than 140 million tons of iron ore, and it consists of two open-pit mines: Weike and Shouyun (referred to as Mine I and Mine II, as in Chen et al. 2015) represented, respectively, in Fig. 1b, c. The mine areas include active extraction sites (about 1.6 km^2 in mine I and 1.5 km^2 in mine II), administrative areas and small villages.

Geologically, the Miyun iron deposit belongs to the Jidong-Mihuai ore concentrated belts in the North China Craton and occurred in the Dacao formation of Miyun Group. The rocks
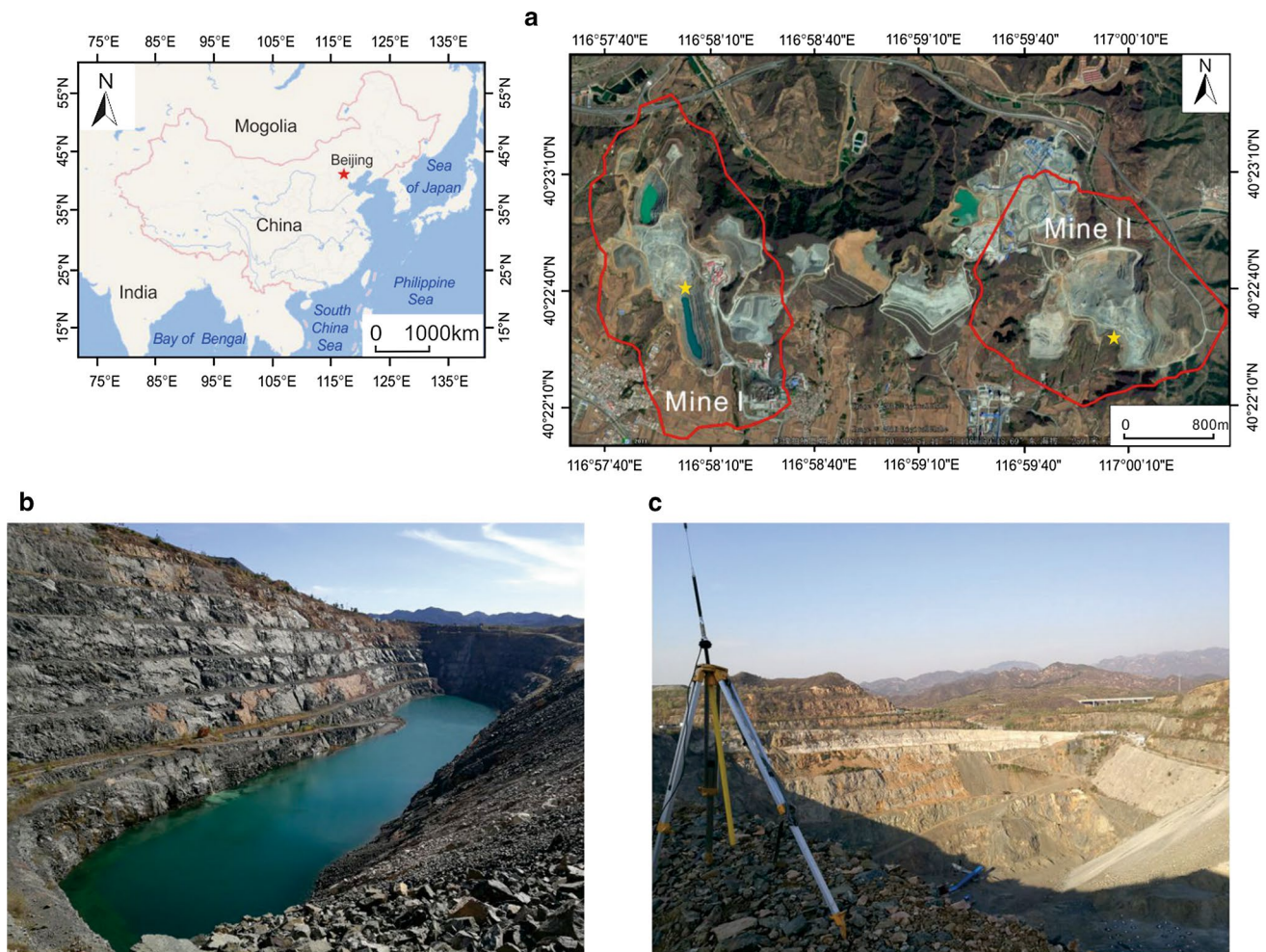
Fig. 1 Location map of the Miyun Iron Mine (**a**) and pictures of the analyzed open-pit mines (Beijing District, People's Republic of China): Mine I (**b**) and Mine II (**c**)

are mostly gneisses, pyroxenites, granulites, and magnetite quartzite. The metallogenic type of this mine is a volcanic-sedimentary metamorphic type, which is an important iron type in the world due to its vast reserves (Zhao et al. 2014; Chen et al. 2016). In its early stage, activities in the mine were mainly underground. After more than 40 years of exploitation, the mine activities switched to open-pit mine in 2010. The natural vegetation in the study area is dominated by grass, about 10–30 cm high. Other vegetation types include a small number of isolated trees with crowns up to ~ 2 m in diameter. There is no vegetation and no grass within the active extraction site, the region of interest for this monitoring project. All these conditions offer the excellent opportunity to perform a UAV survey.

Methodology

Field campaigns and data acquisition

In this study, the Miyun Iron Mine was surveyed by a UAV during two campaigns in August 2014 (Chen et al. 2015) and October 2016. To minimize the sources of the error, we used the same UAV system: an autonomously flying UAV and a camera set to take photographs at a fixed interval automatically. The UAV is a small, fixed-wing UAV (Skywalker X5, Fig. 2b), measuring 0.6 m in length and with a 1.2 m wings span. It can fly for up to 40 min using 4 cell 3500 mA lithium polymer batteries, and it weighs
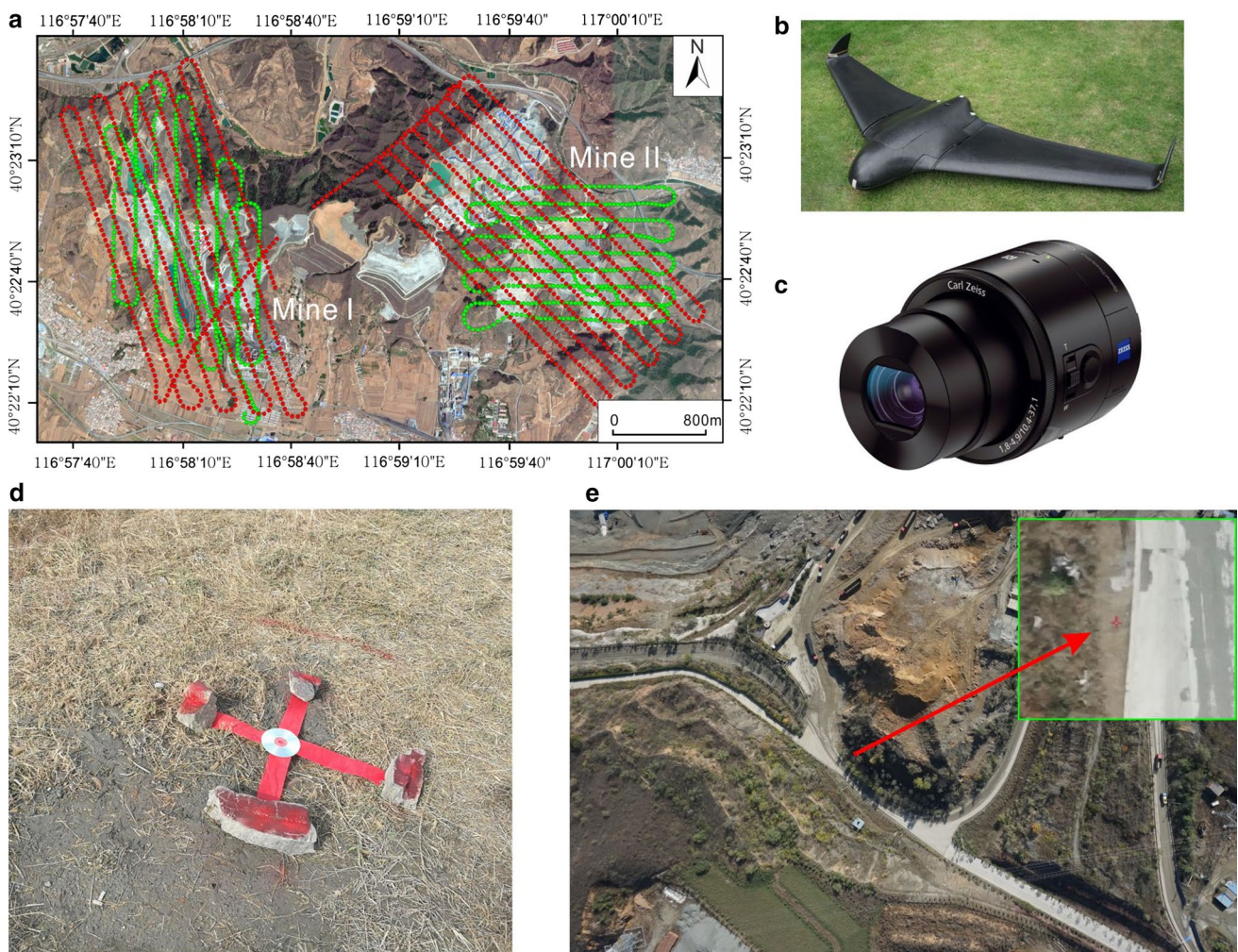
Fig. 2 Field campaigns and data acquisition. **a** The mission planning and location of flight, green and red point represent the trigger point in 2014 (Chen et al. 2015) and 2016, respectively. **b** The Skywalker X5 UAV used in this study. **c** Sony QX100 camera with 20.9 M pixel resolution. **d** Ground control point marked with red cloth and disk. **e** UAV photograph from the October 2016 survey; inset shows a close-up of a GCP in the picture

about 2.5 kg. The camera used was a Sony QX100 camera (20.9 M pixel resolution) (Fig. 2c) with a Carl Zeiss 10.4–37.1 mm lens. The camera was fixed to the UAV using a simple homemade camera mount.

The UAV can be operated both manually by the remote control and autonomously by using an external PC and a flight plan. We designed the flight plan between 250 and 350 m above the ground, with a minimum of 80% overlap for a single stripe and a 40% overlap between stripes. Ten flight lines were set for each of mines. Due to the time limitation of the UAV, the survey was planned separately for the two sites. Based on the fight plan, photographs were

Table 1 Overview of both UAV campaigns in 2014 (Chen et al. 2015) and 2016

UAV campaign		Flight height (relative, m)	Number of pictures	Photointerval (m)	Number of stripes	Stripes interval (m)	Overlap single stripe (%)	Overlap between stripes (%)
Aug. 2014	Mine I	291	437	40	8	190	81	40
	Mine II	267	973	40	9	150	81	62
Oct. 2016	Mine I	353	657	40	10	150	80	52
	Mine II	321	669	40	10	150	80	45

automatically taken. Table 1 shows the detail information about the data acquisition.

Because the photographs from UAV are not associated with any position information, ground control points (GCPs) are required for both relative and absolute topographic accuracy (Cook 2017). For this research, red targets with a centrally located reflector (of about 50 cm, Fig. 2d) were distributed over the Mine to serve as GCPs. In August 2014 Chen et al. (2015) considered 8 GCPs for Mine I and 9 GCPs for Mine II; in October 2016, we used 28 GCPs for Mine I and 7 GCPs for Mine II (Table 2). The location of the GCPs was measured using a dual-frequency RTK DGPS, providing GCP coordinates with an absolute accuracy of 0.02–0.04 m. The dual-frequency RTK DGPS was used to enhance the GPS reading accuracy of coordinates measurements.

Digital elevation model generation

The UAV-collected photographs were processed to obtain orthophotographs and DEMs using the standard SfM workflow (Immerzeel et al. 2014). Some SfM software packages are nowadays available, free or commercial (James and Robson 2012; Hsieh et al. 2016; Messinger et al. 2016). For this study, we applied the Agisoft PhotoScan® software package (version 1.2.5, build 2594, http://www.agisoft.com/). A general overview of the SfM procedure with PhotoScan is described in (Verhoeven 2011). Briefly, this procedure comprises four main steps: (1) Image alignment, by identification of images with common features, solving camera position and reconstructing 3D scene with no information about the spatial scale; (2) Georeferencing, by using the GCPs to improve the absolute accuracy of the bundle adjustment and the 3D model; (3) Optimization of image alignment; (IV) Dense geometry reconstruction. By this last step, it is possible to export both an orthophotograph for a visual interpretation/validation of the results and a dense point clouds for the subsequent processing steps. The software reports the number of tie points, ground resolution and georeferentiation errors obtained by the SfM methodology (Table 2).

The point clouds were further processed using the open source program CloudCompare® (http://www.danielgm.net/cc/), to remove the additional noise. In this study, a filter automatically removed positive and negative outlier points

in CloudCompare®. Further, points clearly outside the range of the elevation values of the mine sites were cleaned manually. Since a separate workflow georeferenced each survey, it was necessary to co-register the datasets to allow a multi-temporal analysis and to evaluate correctly any change. To this point, within CloudCompare®, each pair (for the two surveys) of cleaned point clouds was run with an Iterative Closest Point (ICP) algorithm to estimate the transformation matrices, which include rotational parameters, translation and scale parameters. Each pair of cleaned point clouds (from which the DEMs are created) was co-registered in CloudCompare® using the co-registration matrices. The final co-registered point clouds offered then the basis for the creation of high-resolution (1 m) DEM, based on the natural neighbors interpolation algorithm (Sibson et al. 1981) (Fig. 3).

An assessment of the geometric accuracy was carried out for the two DEMs (for 2014 survey, the readers should refer to Chen et al. 2015). Vertical accuracy of a flat unchanged area was assessed by the use of the RMSE (root mean squared error) considering about 30 checkpoints for each mine. The result shows that the vertical accuracy of DEMs ranges from 0.053 up to 0.055 m, an acceptable error for the geomorphic analysis and in line with previous works on UAV and SfM (Chen et al. 2015; Haas et al. 2016). Using the stable area approach that will be explained in the next subsection, we evaluated the co-registration errors (Westaway et al. 2000). Table 2 reports the georeferentiation and co-registration errors.

DEM of difference (DoD)

The DoD approach subtracts an earlier terrain elevation from a later one, by keeping into account uncertainty (denoted as δz) of the DEMs themselves. The components of δz include measurement errors, sampling bias, and uncertainties due to interpolation methods among others (Wheaton et al. 2010).

For a quantification of the error in DEMs, we assume that the errors of the grid cells follow a normal distribution with a mean of zero. Therefore, the overall DEM error can be expressed by the standard deviation (Haas et al. 2016). Brasington et al. (2003) showed that the propagated

Table 2 Report about the number of tie points, ground resolution, georeferentiation errors and co-registration errors

UAV campaign		Tie points	Ground resolution (m)	GCPs (m)	XY error (m)	Z error (m)	Co-registration error (m)
Mine I	Aug-14	382,238	0.064	8	0.069	0.059	0.523
	Oct-16	585,257	0.056	28	0.058	0.055	
Mine II	Aug-14	399,131	0.081	9	0.054	0.059	0.373
	Oct-16	677,083	0.072	7	0.083	0.053	
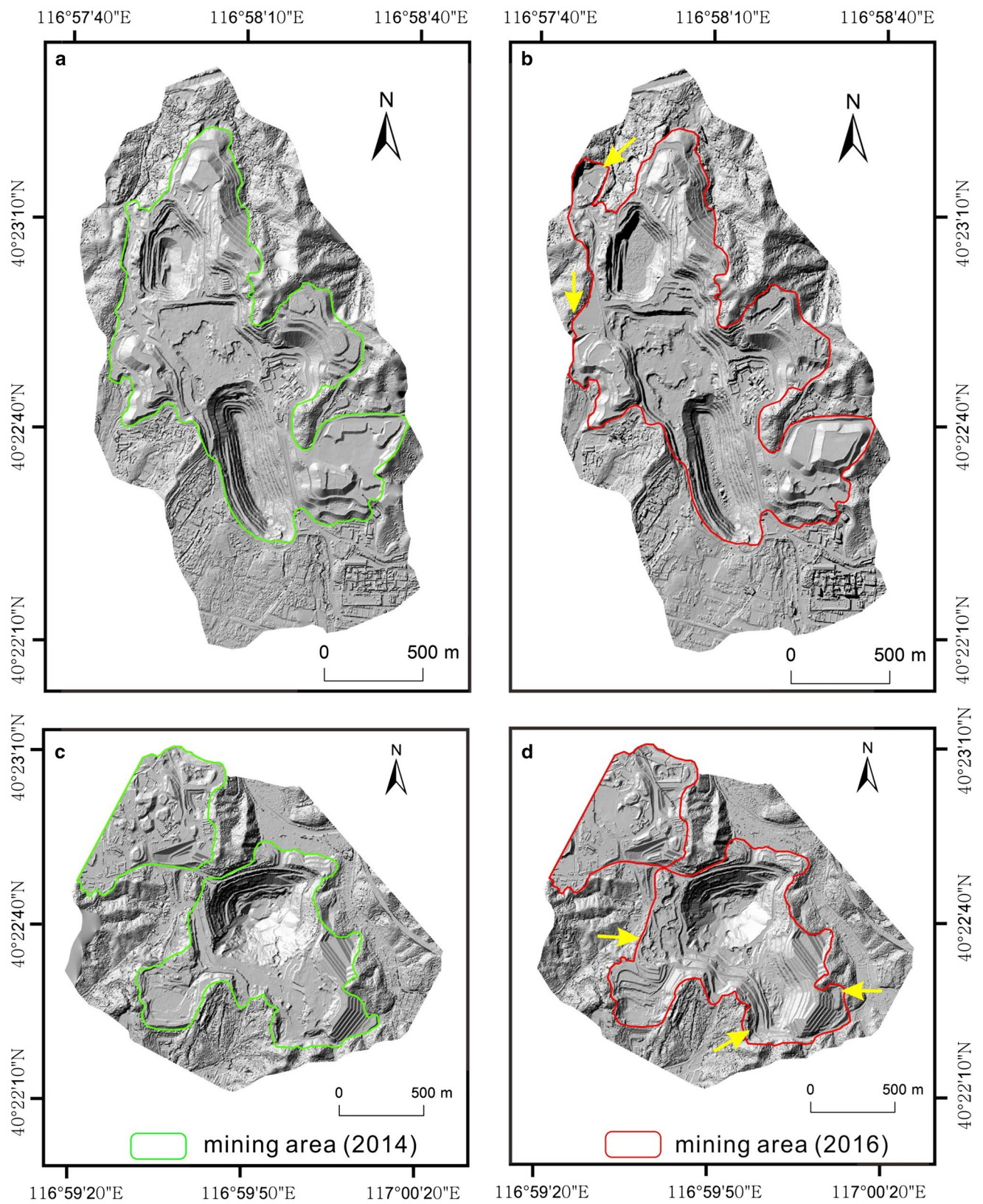
Fig. 3 Digital elevation models (DEMs) at 1 m resolution and mining area (extract from orthophotograph). DEM of **a** Mine I and **c** Mine II generated from the August 2014 survey (Chen et al. 2015); DEM of

b Mine I and **d** Mine II generated from the October 2016 survey; yellow arrow marked the changed extent

uncertainty (δ_{DoD}) into the DoD can be calculated using a Gaussian error propagation as:

$$\delta_{DoD} = \sqrt{\left(\delta z_{new}\right)^2 + \left(\delta z_{old}\right)^2} \qquad (1)$$

where δz_{new} and δz_{old} are the individual errors in DEM_{new} and DEM_{old}, respectively. We assumed that the DoD uncertainty is spatially uniform, and this allows estimating the total volumetric error of all n raster cells with cell size c in the DoD (Lane et al. 2003).

$$\delta_{DoD} \sqrt{nc^2} \qquad (2)$$

In standard DoD analysis using SfM, the use of spatially uniform uncertainty is typical, to distinguish real changes from noise (Brasington et al. 2000; Lane et al. 2003; Wheaton et al. 2010; Prosdocimi et al. 2016; Haas et al. 2016; Sofia et al. 2017). A key limitation of this approach is that the error statistic is averaged across the whole surface. This practice may result in under- and/or overestimates of elevation changes in some parts of the DEM. However, while this is of crucial significance in situations when changes are very subtle in nature, this is suitable if the signal-to-noise ratio is very high (Passalacqua et al. 2015), such as the case of this study or other studies in mining research (Haas et al. 2016). In this case, the dataset is used to differentiate target features on the order of tens of meters in height, and thousands of m^2 in width, compared to an error of ~ 0.5 m. Furthermore, given the acquisition parameters for the surveys, and the DEM generation approach, the assumption of uniform uncertainty is reasonable. To refine the DoD uncertainty, the most commonly adopted procedure involves specifying a level of detection (Lod) to distinguish the real geomorphic changes from noise (Lane et al. 1994, 2003; Brasington et al. 2003; Bennett et al. 2012; Turner et al. 2015). Elevation changes that are beneath the detection limit (Lod) are typically discarded. Meanwhile, those that are above it are treated as real (Prosdocimi et al. 2016).

Brasington et al. (2003) and Lane et al. (2003) show how probabilistic thresholding can be carried out with a user-defined confidence interval. The absolute value of each grid cell in the DoD ($|Z_{new} - Z_{old}|$) is related to δ_{DoD} to calculate a t score. Then, the probability can be calculated by relating the t-statistic to the cumulative distribution function of a t score (Wheaton et al. 2010).

$$t = \frac{|Z_{new} - Z_{old}|}{\delta_{DoD}}. \qquad (3)$$

In Eq. (3), the δ_{DoD} can be estimated by using the stable area approach, and the stable areas are selected from two periods of orthophotograph very carefully. The standard deviation of the original DoD cells in these stable areas represents the value δ_{DoD} from Eq. (2) (Westaway et al. 2000).

In this study, we considered as error the co-registration error of each DEM, and we used a probabilistic thresholding method, with a confidence interval of 95%. We calculated the geomorphic changes by using the Geomorphic Change Detection 6 (GCD 6) toolbar embedded in ArcGIS 10.3, freely downloadable from http://gcd.joewheaton.org/downloads. We analyzed the DoD in the mining areas (extract from the aerial photographs) because vegetation and buildings are present in the area outside the mine, which will influence the accuracy of DEMs. Also, two big holes filled with water in Mine I (Fig. 6a) were masked for the DoD.

## Slope local length of autocorrelation (SLLAC)

Unlike natural geomorphic processes, the work done by humans is focused in specific locations with well-defined intent (Ghosh et al. 2015). In particular, the open-pit mine has a significant characteristic of anthropogenic topographic signatures (e.g., well-organized bench and terraced wall). The second indicator used to analysis the multi-temporal UAV data was the slope local length of autocorrelation (SLLAC) proposed by Sofia et al. (2014), which was successfully applied in mining landscape in Chen et al. (2015). The SLLAC metric quantifies the local self-similarities of slopes based on a 2D cross-correlation between a slope patch and its surrounding areas (Tarolli and Sofia 2016). The SLLAC calculation begins with a slope map derived from the DEM, by computing the slope as a derivative of the biquadratic function proposed by Evans (1980). A moving window (kernel) approach is then used in the subsequent steps (Fig. 4).

Step one, we calculated the correlation R (Fig. 4b) between a slope template (T in Fig. 4a) and its neighbouring area (W in Fig. 4a), by using the formula (Eq. 4) described in (Haralock and Shapiro 1991; Lewis 1995):

$$R_{(i,j)} = \frac{\sum_{u,v} \left(w_{(i+u,j+v)} - \bar{w}_{i,j}\right)\left(T_{u,v} - \bar{T}\right)}{\left(\sum_{u,v}\left(w_{(i+u,j+v)} - \bar{w}_{i,j}\right)^2 \sum_{u,v}\left(T_{u,v} - \bar{T}\right)^2\right)^{0.5}}. \qquad (4)$$

Assuming a kernel W having a size $M \times M$, and a slope template T of size $N \times N$ (Fig. 4), indices (i, j) are the row and column position of each pixel within the W and they are valid in $1 \leqslant i \leqslant (M - N)$ and $1 \leqslant j \leqslant (M - N)$, while indices (u, v) run across $1 \leqslant u \leqslant N$ and $1 \leqslant v \leqslant N$, $\bar{w}$ is the local mean slope of the kernel W underneath the slope patch T whose top left corner lies on pixel (i, j), and $\bar{T}$ is the mean value of the slope patch.

As a second step, the procedure identifies the characteristic length of correlation, by choosing by definition 37% of
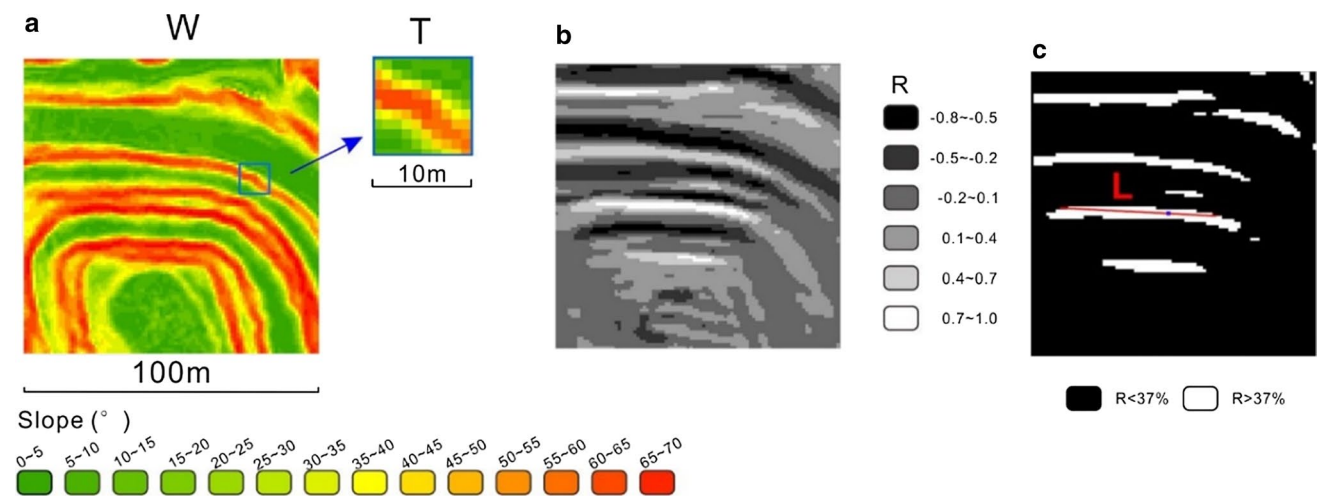
Fig. 4 An example of the calculation of SLLAC for a single moving window (*W*). **a** For each moving window (*W*), a slope template *T* is identified, having the center at the center of *W*. The cross-correlation between *T* and *W* is computed (**b**). The resulting map is thresholded at 37% of its maximum value (**c**). The length of correlation is then the length of the longest line passing through the central pixel (blue dot) and connecting two boundary pixels in the extracted area connected to the central pixel. (The figure is modified, and simplified from Chen et al. 2015)

the maximum correlation value as a threshold according to ISO standards (ISO 2013). As shown in Fig. 4c, the correlation length is the longest line passing through the central pixel, and that connects two boundary pixel in the extracted area. In this study, we applied the kernels identified in (Sofia et al. 2014; Chen et al. 2015). (100 m × 100 m for the moving window and 10 m × 10 m for slope template).

After that, the SLLAC map is produced. For further analysis, the Spc (surface peak curvature) parameter was used to uniquely characterize the SLLAC map (Stout 2000). The Spc is defined as for every peak:

$$\text{Spc} = -\frac{1}{2n} \sum_{i=1}^{n} \left(\frac{\partial^2 z(x,y)}{\partial^2 x} \right) + \left(\frac{\partial^2 z(x,y)}{\partial^2 y} \right). \tag{5}$$

A peak is defined as a pixel where all eight surrounding pixels are lower in value, n is the number of peaks automatically identified within a map, *z* corresponds to the SLLAC value, and *x* and *y* represent the cell spacing (Stout 2000).

Chen et al. (2015) developed a polynomial approach defining a specific relationship between theSpc and the extent of anthropogenic surface within the analyzed area, that follows equation

$$\text{Art}_\% = j_1 \text{Spc}^3 + j_2 \text{Spc}^2 + j_1 \text{Spc} + j_4, \tag{6}$$

where Art% is the percentage of anthropogenic extent, Spc comes from Eq. 5 and j_1–j_4 are empirically derived coefficients with values 2.402e+07, −2.892e+06, 1.087e+05, and −1209 respectively.

From a geomorphometric and geomorphologic perspective, the core idea behind the SLLAC is that human structures and activities lead to more organized and uniform slopes within a neighborhood, rather than natural processes, so slope values are locally highly correlated (longer correlation length). Such correlation is highly organized in space (low Spc, Eq. 5) (Sofia et al. 2016), and this different organization of the topography can be empirically related to the amount of human-made alterations to the terrain (Chen et al. 2015). It is, therefore, possible to automatically track changes in the extent of the mines during time using the polynomial approach.

Further, in this study, we considered m-times the standard deviation of the SLLAC (σ_{SLLAC}) as the threshold for the recognition of the mining area. To assess the quality of the automatic extraction of the mining area, we used a quality index (Heipke et al. 1997).

$$Q = \frac{\text{TP}}{(\text{TP} + \text{FP} + \text{FN})} \tag{7}$$

where true positive (TP) represents the extracted pixels that are within the mining area; false positive (FP) represents the extracted pixels that lie outside the mining area; false negative (FN) represents the pixels within the mining area that are not extracted.

Result and discussion

DoD analysis

Figure 5 shows the obtained DoD map and the histogram of areal and volumetric elevation change distributions (ECDs) for the two mines.

In Eq. (3), the δDoD can be estimated by using the stable area approach (the δDoD for Mine I is 0.523 m, and for Mine, II is 0.373 m). Figure 5a and Fig. 5b refer to the thresholded DoD map according to a spatially uniform Lod (Lod = 0.129 m for Mine I, Lod = 0.094 m for Mine II). The elevation changes range between 45 to − 49 m for mine I and between 25 to − 83 m for mine II.

The main extraction areas are distributed in the central part of Mine I (Fig. 5c), and the southeastern part of Mine II (Fig. 5d). The elevation changes in this area of Mine I range between − 20 to − 40 m. The average elevation change in the specific area of Mine II is about − 70 m: this location witnessed the creation of well-organized terraced walls. These volumetric changes mainly represent the extracted ore. For Mine I, the main accumulation areas are located in the southeast part (Fig. 5e), which is the tailings dump. The elevation changes in this area range between 20 to 40 m. For Mine II, the main accumulation areas are in the central and north-western part, and they do not refer to a specific tailing dump. In these accumulation areas, the volumetric changes mainly represent the increase of the tailings in the two considered years.

The areal elevation change distributions (ECDs) are histograms showing the total area experiencing a given magnitude of elevation change in each bin, and the volumetric ECDs reflecting the area multiplied by the magnitude of elevation change (Wheaton et al. 2010). The areal ECDs (Fig. 5f, h) have a high peak roughly corresponding to an elevation change of 0 m, but they are mostly asymmetrical. Mine I appears more balanced than Mine II, comparing their accumulation and extraction (45 to − 49 m for Mine I and 25 to − 83 m for Mine II). Mine I has a second peak around − 30 m and a third peak about − 40 m (Fig. 5f). Mine II has a series of small peaks (such as − 14, − 23, − 68 m). These peaks have highly correlated with the procedure of open-pit mining. This is because, during the extraction procedure, the bench of the pit was generated with 10–15 m high. The volumetric ECDs dramatically amplified the peaks far away from zero and reduced the peaks near zero, because these are multiplied by different elevation changes (Fig. 5g, i). Due to discarding DoDs whose elevation changes are beneath the detection limit (Lod), there is some information lost in the DoD map. The yellow and green histograms represent the discarded information of extraction and accumulation, respectively.

Table 3 reports the areal and volumetric DoDs, the mined ore tonnage, and the tailings tonnage for the two mines.

These results prove in quantitative terms what emerged visually from Fig. 5. We can calculate the loss of information by subtracting the LoD from the Raw in Table 3. In this regard, the change of area for Mine I is 75,835 m^2 (35,657 m^2 for the extraction area, and 40,178 m^2 of the accumulation area), and for Mine, II is 69,975 m^2 (34,897 m^2 for extraction area, and 35,078 m^2 for accumulation area).

The DoDs of two mines entail a net negative volume, which is in line with the fact that the two mines remained active during these 2 years. The geomorphic changes could be used to quantitative assessments of the mined tonnage and the tailings tonnage. The extraction volume mainly represents the volume of the extraction ore, which if multiplied by the average ore-bearing rate, density and ore grade could represent the mined ore tonnage. Similarly, we can estimate the tailings tonnages by using the accumulation volume multiplies the density of residues. For example, we estimated the mined tonnage and the tailings tonnage (Table 3) by the related parameters (the average of ore-bearing rate of about 20%; the average ore grade of about 30%; the average density of iron ore of about 4 t/m^3, and the density of tailings of about 2.5 t/m^3). As to the volume errors, Mine II show smaller errors than Mine I. This is because Mine II has a smaller Lod and detectable area.

SLLAC analysis

Figure 6 shows the SLLAC map obtained from UAV DEMs for the two mines in 2014 and 2016.

As we can see, the SLLAC map texture is characterized by the elongated elements, defined as fibers in Sofia et al. (2014). These fibers are mainly located within the mining area, and a higher degree of order is visible corresponding to the terraces walls. Moreover, the higher the Spc, the lower the area within the study site covered by terraces (Sofia et al. 2014; Chen et al. 2015). In this regard, the two mines have a Spc of 0.038 m^{-1} (Mine I) and 0.039 m^{-1} (Mine II) in 2014, and 0.037 m^{-1} (Mine I) and 0.038 m^{-1} (Mine II) in 2016. By using the polynomial approach (Chen et al. 2015), the terraced surface increased from 63 to 70% for mine I, and from 56 to 63% for mine II. It means an increase of mining areas about 0.24 km^2 for Mine I and 0.21 km^2 for Mine II. However, the areal changes do not come only from the open-pit mine itself, when comparing the mining areas extract from the orthoimages. The yellow arrow marked the modified area of the open-pit mine in Fig. 6, and we can measure a total mining area changes of about 0.07 km^2 for both mines. Other anthropogenic elements (roads and buildings) contribute to creating fibers on the SLLAC. Thus they are included in the Spc evaluation. For example, in the northeastern part of Mine II, there is some highway captured
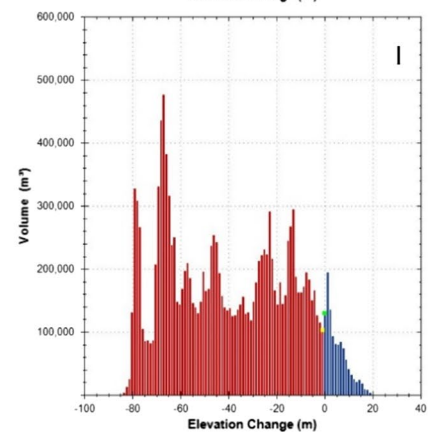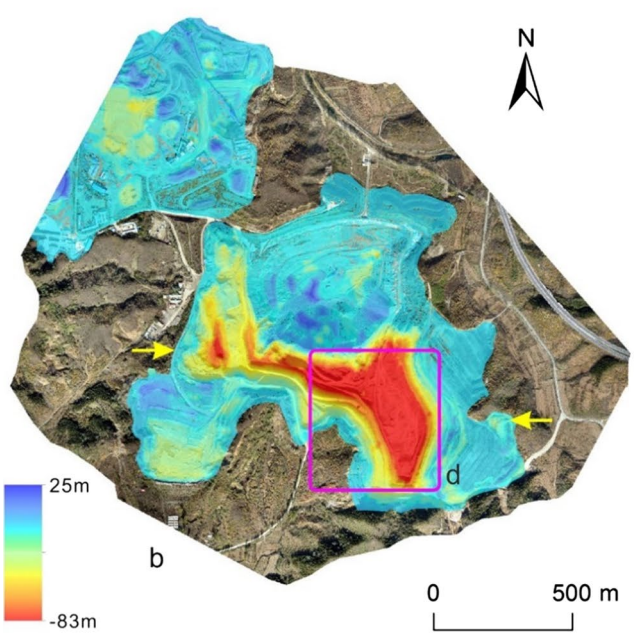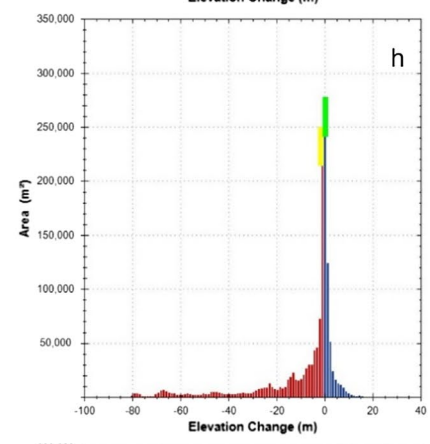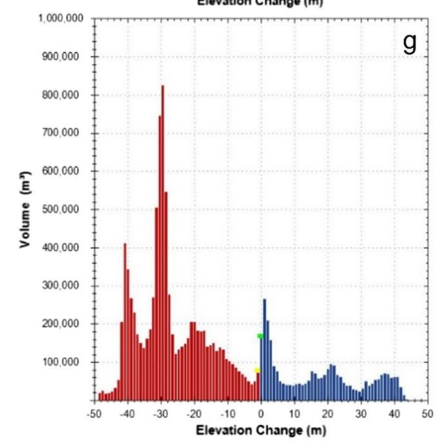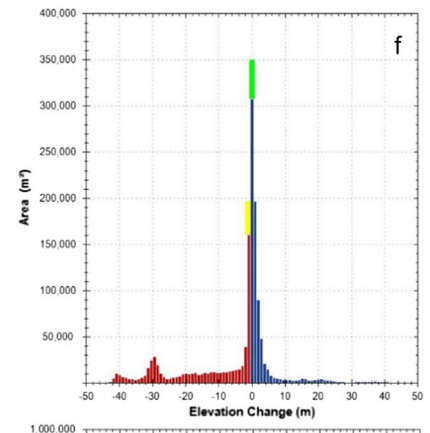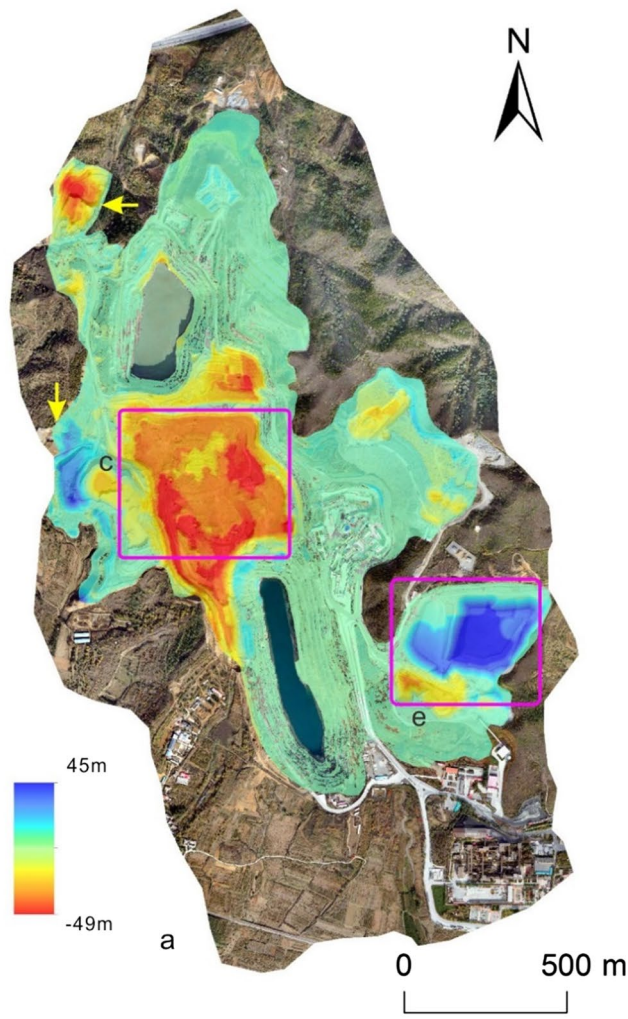
◄**Fig. 5** DEMs of difference (DoD) for the period from 2014 to 2016. **a**, **b** Thresholded DoD according to Lod; **c**, **d** main production areas for Mine I and II: **e** a tailings dump for Mine I: **f**, **h** areal ECDs for Mine I and Mine II; **g**, **i** volumetric ECDs for Mine I and Mine II; yellow arrow marked the changed extent; the yellow and green histogram represent the discarded information

by the DEM that represents high SLLAC value (Fig. 6c, d). Another example is the southeastern part of Mine I; there are buildings and roads that belong to the company (Fig. 6a, b). By including all of the anthropogenic surfaces, the result of the empirical model is in line with the resulting extract from the orthoimage (Chen et al. 2015). Figure 7 shows the boxplot of SLLAC values considering the area inside the mine as compared the area outside the pit for mining sites I and II in 2014 and 2016.

As we can see, the difference of SLLAC is evident in both mines, for both time frames. It is clear that areas within the mines have a higher mean SLLAC if compared to areas outside. For Mine I, the median SLLAC within the mined area is 43.43 m in 2014 and 38.63 m in 2016, and the median value outside the mined area is 9.22 m in 2014 versus 11.72 m in 2016. For Mine II, the inside median SLLAC is 35.17 m in 2014 versus 34.02 m in 2016, while the outside median value is 12.19 m in 2014 and 7.29 m in 2016, respectively. Also, areas within the mine have a higher SLLAC variability than the area outside the pit, as represented by the IQR box in the boxplot. In this regard, for the Mine I, the IQR of areas in mine varies from 55.25 m in 2014 to 55.78 m in 2016, while the outside IQR is 18 m in 2014 and 20.75 m in 2016. For the Mine II, the inside IQR varies from 47.21 m in 2014 to 55.22 m in 2016, while the outside IQR is 21.01 m in 2014 and 14 m in 2016. The reason for these differences is that the mining area has a well-organized terraced wall and different physical lengths. In contrast, vegetation and buildings create small and scattered shapes in the area outside the mine.

Considering the change of SLLAC from 2014 to 2016, for the area within the Mine I, the median of SLLAC decreased. This is because there were no terraces built in main extraction area (Fig. 9c, d). Instead, the increasing water levels detract the original terraced wall (Fig. 6a, b). The IQR and median of SLLAC of outside the Mine I increased, because there are some road and buildings in the south part of Mine I captured by the DEM. For the Mine II, the SLLAC of inside mine seems few changes, but the IQR and median of SLLAC of outside decreased, this is because the expanded boundary of mine reduced the noise related to the road (yellow arrow in Fig. 6d).

Figure 8 shows the extraction result by using m-times standard deviation as the threshold and the quality index (Q).

As we can see, with the increase in m, the Q becomes smaller. However, by using only one time the standard deviation, the extraction appears very noisy. On the other hand, not enough information is left to depict the boundary of the mine by using three times the standard deviation. When using the 1.5–2.5 times standard deviation as the threshold, the extent of the mining area is correctly extracted. For Mine I, because there are too many road and buildings in the south part, the optimum extraction is obtained by using 2.5 (or 2) times the standard deviation as a threshold to reduce the noise. For Mine II, some similar results are obtained applying 1.5 (or 2) times the threshold. Therefore, we recommend 2 times the standard deviation of SLLAC as an indicative measure to extract the extent of the open-pit mine.

Discussion

Considering the results obtained with the DoD and SLLAC (see Fig. 9 for details), we can affirm that both of them are robust method to detect the geomorphic changes in open-pit mining and to monitor the whole mining production process, when remote sensing multi-temporal data (e.g., UAV surveys) are available. Comparing to the previous works about the quantification and analysis of geomorphic processes in mining areas, some similarities and differences arises. This research is using multi-temporal SLLAC to automatically detect the extent of the mine, both in terms of coverage (through the Spc approach), and in terms of location of the terraces (through the thresholding approach). Previous works in the literature (e.g., Haas et al. 2016; Esposito et al. 2017) estimated the volumetric changes in the mines, but the approach was not automatic.

The DoD is an already established method in literature, while the SLLAC is an approach proposed to characterize surface morphologies (Sofia et al. 2014) for agricultural terraces detection. We can summarize advantages and critical issues of the two methods as follows:

- *Consistency* The main changed surfaces are related to the high value of DoD and SLLAC changes. However, the two metrics are not correlated. For example, the change of SLLAC appears to be small in the central part of the changed areas. This is because terraces are always distributed around the mining area, rather than in the flat part at the center of the mining area.
- *Changes* Given multi-temporal DEMs, the SLLAC could calculate the areal changes of the open-pit by extracting its extent. The Spc could estimate the areal change of the anthropogenic surface by using the polynomial approach. The DoD could calculate the volumetric changes, while the areal change of DoD means the detectable area (elevation change beyond the Lod). Indeed, the SLLAC is

Table 3 Report about the areal and volumetric DoD, the mined ore tonnage and the tailings tonnage for two mines

Attribute	Mine I			Mine II		
	Raw	Thresholded	Error	Raw	Thresholded	Error
Extraction area (m^2)	685,087	649,430	NA	911,034	876,137	NA
Accumulation area (m^2)	831,600	791,422	NA	550,494	515,416	NA
Change of area (m^2)	1,516,687	1,440,852	NA	1,461,528	1,391,553	NA
Extraction volume (m^2)	9,188,963	9,186,694	±83,582	13,974,619	13,973,070	±78,852
Accumulation volume (m^2)	3,093,291	3,090,662	±101,856	1,129,807	1,128,240	±46,387
Total net volume (m^2)	−6,095,672	−6,096,032	±131,759	−12,844,812	−12,844,831	±91,485
The mined ore tonnage (t)	2,205,351	2,204,806	±20,060	3,353,908	3,353,537	±18,924
The tailings tonnage (t)	7,733,227	7,726,655	±254,640	2,824,517	2,820,600	±115,967

Raw represent unthresholded DoD
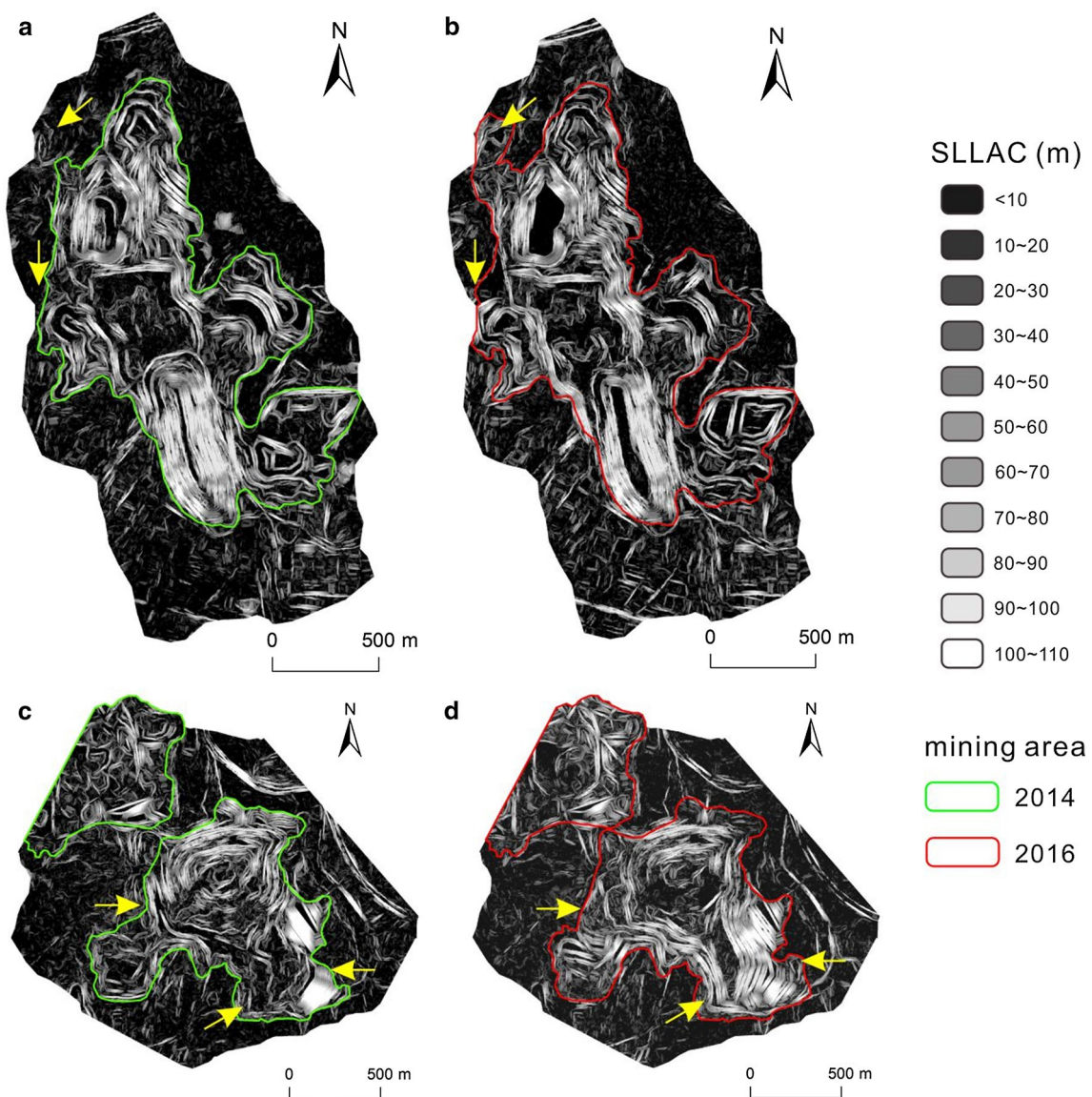
Fig. 6 SLLAC maps for mining sites I and II in 2014 and 2016. Mine I SLLAC: **a** in 2014 and **b** in 2016; Mine II SLLAC: **c** in 2014 and **d** in 2016; yellow arrow marked the changed extent
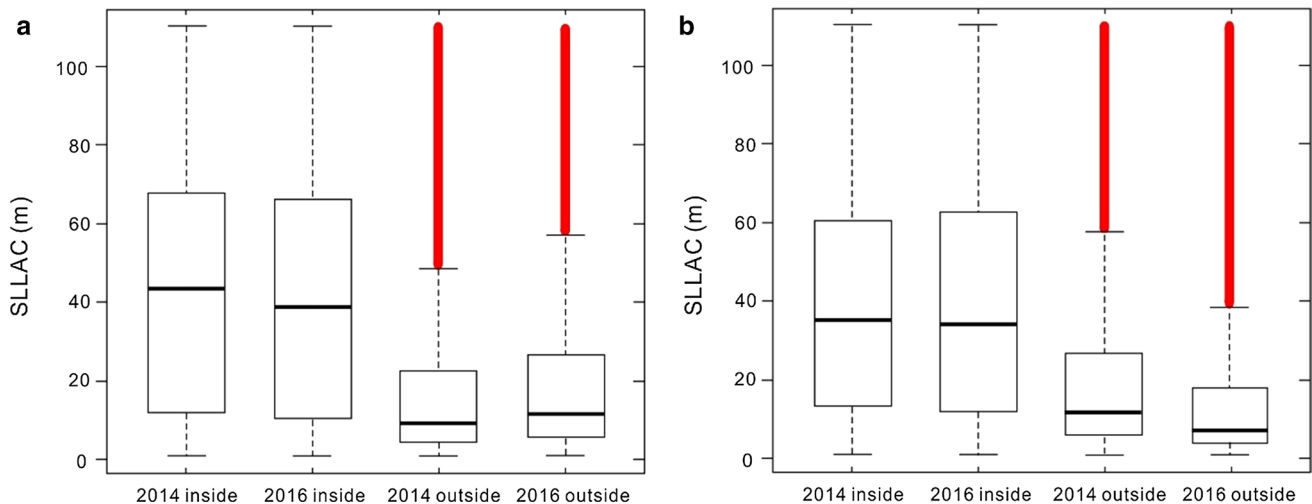
Fig. 7 A boxplot of SLLAC values considering the area inside the mine as compared the area outside the mine in 2014 and 2016. **a** Correspond to Mine I and **b** refer to Mine II

able to detect the geomorphic changes in the horizontal direction and the DoD in the vertical direction.

- *Accuracy* The SLLAC is easily influenced by anthropogenic elements in general (roads, buildings, etc.), and the accuracy of the extracted extent of about 28–35% (using 2 times the standard deviation as a threshold, Fig. 8). This value is, however, higher than other works dealing with feature extractions in other contexts (Tarolli et al. 2012; Sofia et al. 2016). The error of DoD comes mainly from the uncertainty in the DEM and the co-registration error. The percentage of volumetric error is about 1–4% (Table 3).

Summarizing, SLLAC could be used to extract the extent of open pit, due to its sensitiveness to the terraced walls, which are always located around the open pit. The Spc helps to provide a suitable estimation of the percentage of the anthropogenic surface by using the polynomial approach, proposed by Chen et al. (2015). While such extraction is affected by some noise due to other anthropogenic features that could be present on the surface (e.g., roads), it can be useful for large-scale analysis where the purpose is to analyze the topographic signature human activities (Tarolli et al. 2017). A 2D automatic classification of features from a purely computational point of view, might be achieved in multiple ways, and the use of remote sensing in mining areas has been widely used to characterize land cover changes (Esposito et al. 2017), using methods that include change detection algorithms from imagery, and compound analyses, e.g., (Townsend et al. 2009; Asner et al. 2013). Other detection algorithms also exist in the literature, for different target objects (e.g., roughness analysis, or geostatistics). However, these classifications produce classes of homogeneous

identities that do not necessarily refer to useful information (such as specific land uses). Thus expert criteria are needed (interpretation of the results) to identify further which class corresponds, for example, to the mining area. As well, the presence of vegetation and other objects on the surface may degrade the DEM for the purpose of identifying a specific feature. The SLLAC and the derived Spc allows to quantify directly a percentage of anthropogenic surface, and this has been tested in multiple natural Vs. artificial landscapes, thus it is more robust and objective. On the other hand, within the mining area, the DoD can provide a detailed quantification of areal and volumetric changes by subtracting an earlier terrain elevation from a later one. The usefulness of DoD for geomorphic change detection is a confirmation on what the Earth science community has been highlighting in the last few years: the importance of using multi-temporal DEMs. Respect to other works (Esposito et al. 2017; McLeod et al. 2013; Hugenholtz et al. 2015; Lee and Choi 2015; Shahbazi et al. 2015), using a DEM approach is quicker, and easier to handle than using point clouds. As well, the high number of values in a point cloud does not necessarily define a better topographic information respect the 2.5D information contained in a DEM. With the progressive advances and improvements of remote sensing techniques, multi-temporal analysis of Earth surface processes and their quantification using DEM, among other approaches, will be one of the Earth science challenges in the future (Tarolli 2014).

This work, Esposito et al. (2017), focuses on changes due to mechanisation and human activities, rather than to natural processes, and we underlined an extension and deepening of the mining areas during the years. As found in (Hu et al. 2017) deformation in the local mining area can expand to the surrounding areas. Our results suggest
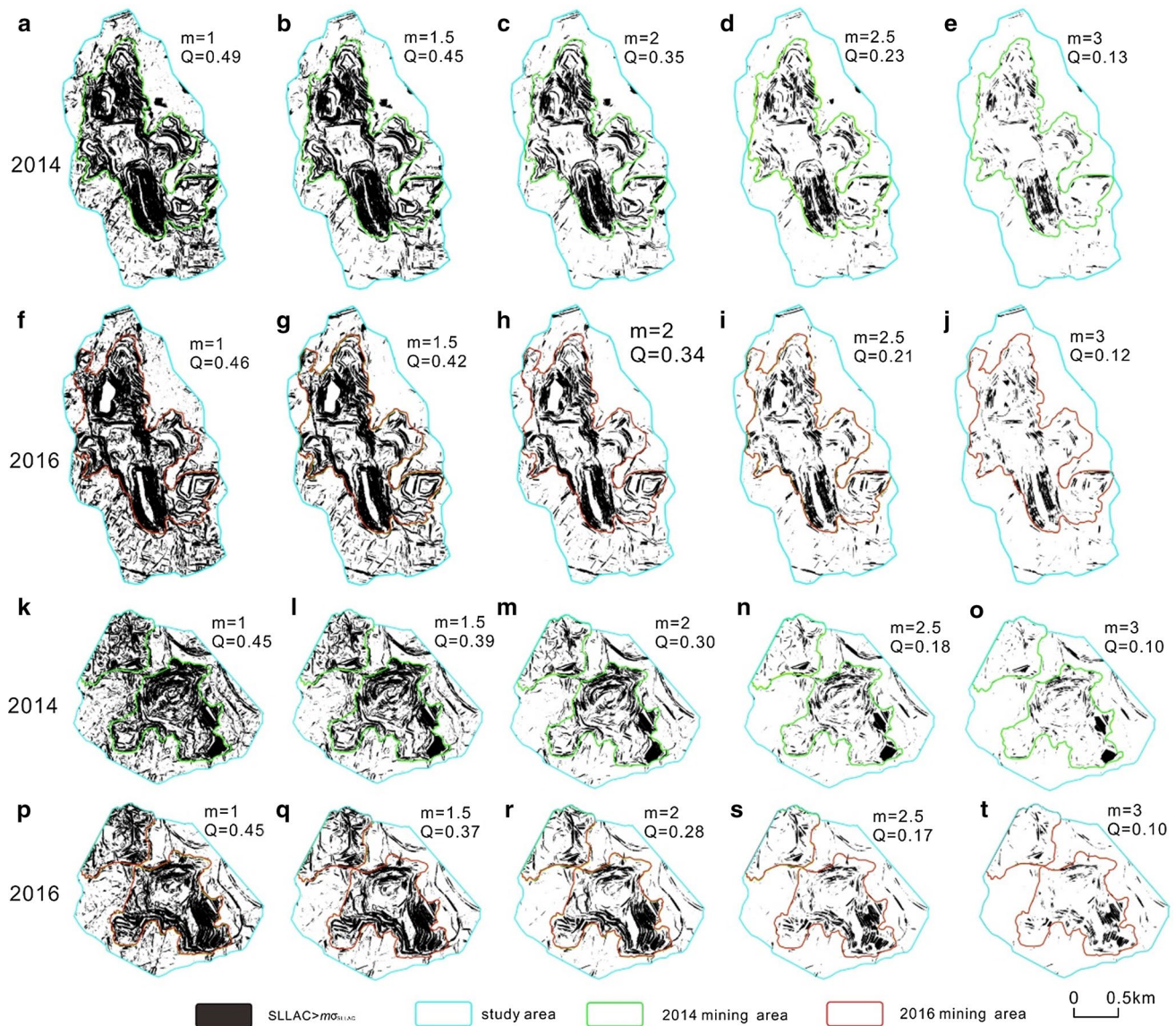
Fig. 8 Areas having correlation lengths larger than *m* standard deviation of SLLAC for mining sites I and II in 2014 and 2016 (*m* represent the *m*-times standard deviation; *Q* represent the quality index)

that acute deformation such as large movements of materials is greater in magnitude, with respect to the material moved by natural erosive/depositional processes in abandoned mines. These large-scale changes can be automatically monitored using DSMs derived from SfM. (Hancock et al. 2006, 2008; Haas et al. 2016) highlighted how geomorphic processes in closed mines lead not only to high amounts of erosion and deposition, but also to changes in the hydrological conditions. To add to these results, this research shows that a careful scrutiny of the human-induced changes is critical and should be used as a basis to predict further changes to processes, to prevent possible damages or disasters caused by ground deformation.

Final remarks

Open-pit mining has a significant influence on the environment. This contribution provides a useful framework for monitoring open-pit mines and for a better understanding of mining environmental effects. It could also be useful for a sustainable environmental planning. Two open-pit mines near Beijing (People's Republic of China) were considered as study areas. The analysis demonstrated that unmanned aerial vehicle (UAV), as a robust and low-cost technique, could be used routinely to collect a substantial time series of data, and to generate, using structure from
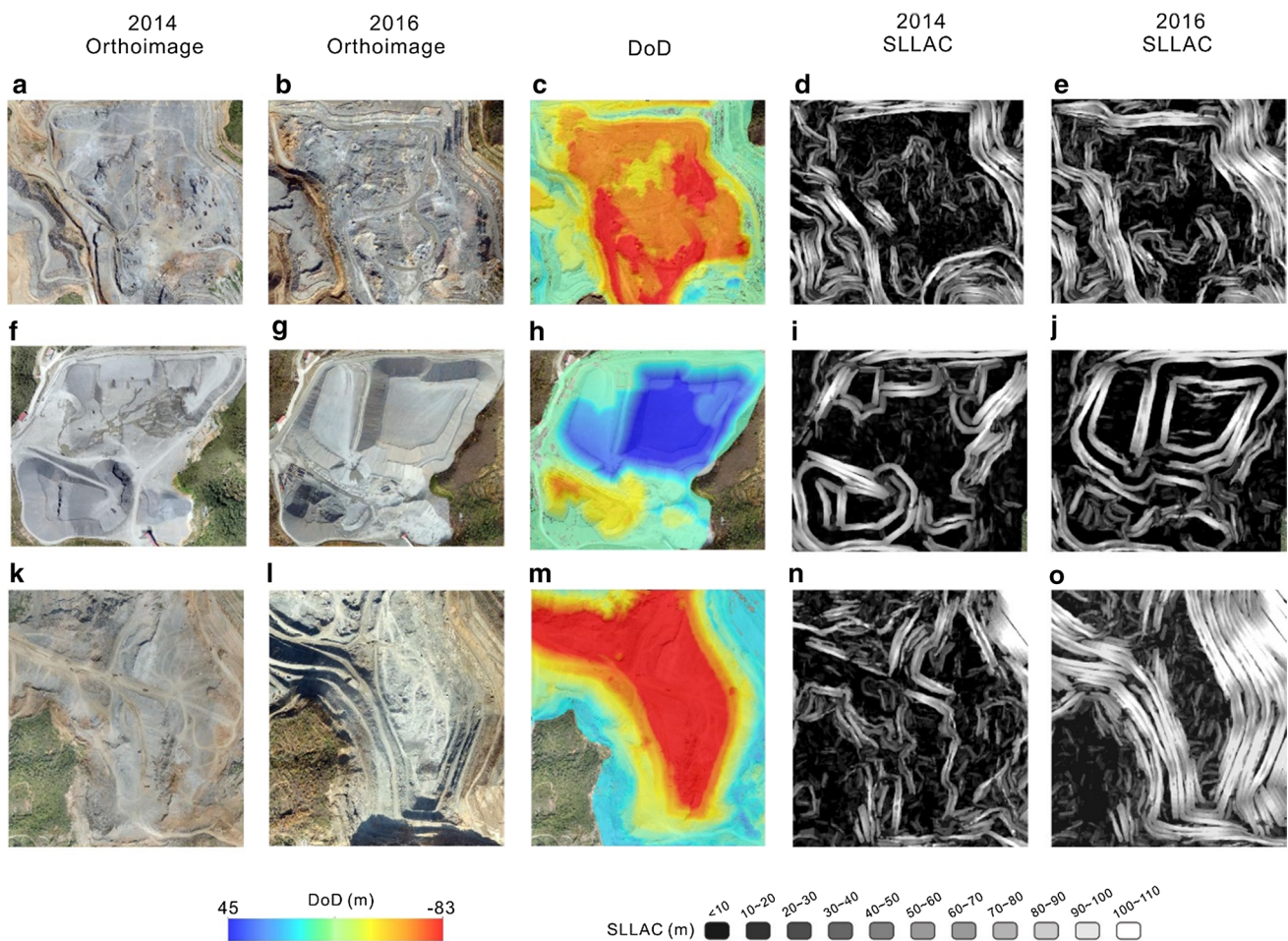
Fig. 9 Details of the DoD and SLLAC in the areas subject to terrain extraction and accumulation. **a–e** Terrain extraction area of Mine I; **f–j** terrain accumulation area of Mine I; **k–o** terrain extraction area of Mine II

motion photogrammetry, accurate DEMs to monitor the open-pit mine. While this result should be obvious looking at the recent literature on the application of UAV, the real achievement of this study was the geomorphic changes analysis and their quantification using two methodologies: DoD (DEM of Difference) and SLLAC (slope local length of autocorrelation). The analysis of the DoD, a well-established method in the Earth science community, allowed for the areal changes and the volumetric changes. This information should help mining companies to do thoughtful planning for production and environmental recovery. The analysis of the SLLAC and its derived parameters (Spc, Surface Peak Curvature) allows for a detailed depiction of terraces, and of the extent of the open-pit mine. Other geomorphometric approaches (e.g., local spectral analysis, wavelets, and image texture approaches) might be followed for a 2D identification of the mine extent; however, they require expert criteria (interpretation of the results) to fully identify the feature of interest. The SLLAC and the derived Spc allow to quantify directly a percentage

of anthropogenic surface and thus is suitable for a quick estimate over time. Also, due to the ability of the SLLAC to detect the terraces, it could be used for future monitoring of the stability of terraces within the mines, without requiring additional datasets (e.g., imagery, other geomorphic parameters). Once the hazards happen (e.g., slope failure), we can quickly detect it. The step forward for this work will involve continuous improvement of the accuracy, e.g., the accuracy of DEMs and co-registration, and also the accuracy of auto-extracting the extent of the mining area.

The methodology described in this paper advances the knowledge in that it offers a convenient tool to assess the open-pit mine's state rapidly and efficiently. This tool makes it possible to get high-resolution topographic information during the entire mine's life. Based on this information and the application of the DoD and SLLAC, it is possible to understand in details of the morphological dynamics of a mine's life. Therefore, this could provide a substantial time series datasets (such as orthophotograph, DEM, geomorphic

changes), which could be used to support sustainable environmental planning and/or to mitigate the consequences of anthropogenic alterations due to mining.

References

Asner GP, Llactayo W, Tupayachi R, Luna ER (2013) Elevated rates of gold mining in the Amazon revealed through high-resolution monitoring. Proc Natl Acad Sci USA 110:18454–18459. https://doi.org/10.1073/pnas.1318271110

Bennett GL, Molnar P, Eisenbeiss H, Mcardell BW (2012) Erosional power in the Swiss Alps: characterization of slope failure in the Illgraben. Earth Surf Process Landf 37:1627–1640. https://doi.org/10.1002/esp.3263

Brasington J, Rumsby BT, McVey RA (2000) Monitoring and modelling morphological change in a braided gravel-bed river using high resolution GPS-based survey. Earth Surf Process Landf 25:973–990. https://doi.org/10.1002/1096-9837(200008)25:9<973:AID-ESP111>3.0.CO;2-Y

Brasington J, Langham J, Rumsby B (2003) Methodological sensitivity of morphometric estimates of coarse fluvial sediment transport. Geomorphology 53:299–316

Brown AG, Tooth S, Bullard JE et al (2017) The geomorphology of the Anthropocene: emergence, status and implications. Earth Surf Process Landf 42:71–90. https://doi.org/10.1002/esp.3943

Chen J, Li K, Chang KJ et al (2015) Open-pit mine geomorphic changes analysis using multi-temporal UAV survey. Int J Appl Earth Obs Geoinf 42:76–86. https://doi.org/10.1016/j.jag.2015.05.001

Chen J, Xiang J, Hu Q et al (2016) Quantitative geoscience and geological big data development: a review. Acta Geol Sin 90:1490–1515. https://doi.org/10.1111/1755-6724.12782

Colomina I, Molina P (2014) Unmanned aerial systems for photogrammetry and remote sensing: a review. ISPRS J Photogramm Remote Sens 92:79–97. https://doi.org/10.1016/j.isprsjprs.2014.02.013

Cook KL (2017) An evaluation of the effectiveness of low-cost UAVs and structure from motion for geomorphic change detection. Geomorphology 278:195–208. https://doi.org/10.1016/j.geomorph.2016.11.009

Ellis EC (2011) Anthropogenic transformation of the terrestrial biosphere. Philos Trans A Math Phys Eng Sci 369:1010–1035. https://doi.org/10.1098/rsta.2010.0331

Eltner A, Kaiser A, Castillo C et al (2016) Image-based surface reconstruction in geomorphometry-merits, limits and developments. Earth Surf Dyn 4:359–389. https://doi.org/10.5194/esurf-4-359-2016

Esposito G, Mastrorocco G, Salvini R et al (2017) Application of UAV photogrammetry for the multi-temporal estimation of surface extent and volumetric excavation in the Sa Pigada Bianca open-pit mine, Sardinia, Italy. Environ Earth Sci 76:103. https://doi.org/10.1007/s12665-017-6409-z

Evans IS (1980) An integrated system of terrain analysis and slope mapping. Z Geomorphol 36:274–295

Fernández T, Pérez JL, Cardenal J et al (2016) Analysis of landslide evolution affecting olive groves using UAV and photogrammetric techniques. Remote Sens 8:837–865. https://doi.org/10.3390/rs8100837

Francioni M, Salvini R, Stead D et al (2015) An integrated remote sensing-GIS approach for the analysis of an open pit in the Carrara marble district, Italy: slope stability assessment through kinematic and numerical methods. Comput Geotech 67:46–63. https://doi.org/10.1016/j.compgeo.2015.02.009

Ghosh R, Chakraborty D, Halder M, Baidya TK (2015) Manganese mineralization in Archean greenstone belt, Joda-Noamundi sector, Noamundi basin, East Indian Shield. Ore Geol Rev 70:96–109. https://doi.org/10.1016/j.oregeorev.2015.04.007

Haas F, Hilger L, Neugirg F et al (2016) Quantification and analysis of geomorphic processes on a recultivated iron ore mine on the Italian island of Elba using long-term ground-based lidar and photogrammetric SfM data by a UAV. Nat Hazards Earth Syst Sci 16:1269–1288. https://doi.org/10.5194/nhess-16-1269-2016

Hancock GR, Grabham MK, Martin P et al (2006) A methodology for the assessment of rehabilitation success of post mining landscapes–sediment and radionuclide transport at the former Nabarlek uranium mine, Northern Territory, Australia. Sci Total Environ 354:103–119. https://doi.org/10.1016/j.scitotenv.2005.01.039

Hancock GR, Crawter D, Fityus SG et al (2008) The measurement and modelling of rill erosion at angle of repose slopes in mine spoil. Earth Surf Process Landf 33:1006–1020. https://doi.org/10.1002/esp.1585

Haralock RM, Shapiro LG (1991) Computer and robot vision. Addison-Wesley Longman Publishing Co., Inc, Boston

Heipke C, Mayer H, Wiedemann C, Jamet O (1997) Automated reconstruction of topographic objects from aerial images using vectorized map information. Int Arch Photogramm Remote Sens 23:47–56

Hsieh YC, Chan YC, Hu JC (2016) Digital elevation model differencing and error estimation from multiple sources: a case study from the Meiyuan Shan landslide in Taiwan. Remote Sens. https://doi.org/10.3390/rs8030199

Hu W, Wu L, Zhang W et al (2017) Ground deformation detection using China's ZY-3 stereo imagery in an opencast mining area. ISPRS Int J Geo-Inf 6:361. https://doi.org/10.3390/ijgi6110361

Huang X, Zhu Y, Ji H (2013) Distribution, speciation, and risk assessment of selected metals in the gold and iron mine soils of the catchment area of Miyun Reservoir, Beijing, China. Environ Monit Assess 185:8525–8545. https://doi.org/10.1007/s10661-013-3193-4

Hugenholtz CH, Walker J, Brown O, Myshak S (2015) Earthwork volumetrics with an unmanned aerial vehicle and softcopy photogrammetry. J Surv Eng 141:6014003. https://doi.org/10.1061/(ASCE)SU.1943-5428.0000138

Immerzeel WW, Kraaijenbrink PDA, Shea JM et al (2014) High-resolution monitoring of Himalayan glacier dynamics using unmanned aerial vehicles. Remote Sens Environ 150:93–103. https://doi.org/10.1016/j.rse.2014.04.025

ISO B (2013) 25178-2: geometrical product specifications (GPS)-surface texture: areal-part 2: terms, definitions and surface texture parameters

Jaakkola A, Hyyppä J, Kukko A et al (2010) A low-cost multi-sensoral mobile mapping system and its feasibility for tree measurements. ISPRS J Photogramm Remote Sens 65:514–522. https://doi.org/10.1016/j.isprsjprs.2010.08.002

James MR, Robson S (2012) Straightforward reconstruction of 3D surfaces and topography with a camera: accuracy and geoscience application. J Geophys Res Earth Surf. https://doi.org/10.1029/2011jf002289

Kobayashi H, Watando H, Kakimoto M (2014) A global extent site-level analysis of land cover and protected area overlap with mining activities as an indicator of biodiversity pressure. J Clean Prod 84:459–468. https://doi.org/10.1016/j.jclepro.2014.04.049

Lane SN, Richards KS, Chandler JH (1994) Developments in monitoring and modelling small-scale river bed topography. Earth Surf Process Landf 19:349–368

Lane SN, Westaway RM, Hicks DM (2003) Estimation of erosion and deposition volumes in a large, gravel-bed, braided river using synoptic remote sensing. Earth Surf Process Landf 28:249–271. https://doi.org/10.1002/esp.483

Lee S, Choi Y (2015) Topographic survey at small-scale open-pit mines using a popular rotary-wing unmanned aerial vehicle (drone). Tunn Undergr Space 25:462–469

Lewin J, Macklin MG (2014) Marking time in geomorphology: should we try to formalise an Anthropocene definition? Earth Surf Process Landf 39:133–137. https://doi.org/10.1002/esp.3484

Lewis JP (1995) Fast template matching. Vision interface 95, Canadian image processingand pattern recognition society. Quebec City, Canada, May 15–19, pp 120–123

Lucieer A, de Jong SM, Turner D (2014) Mapping landslide displacements using structure from motion (SfM) and image correlation of multi-temporal UAV photography. Prog Phys Geogr 38:97–116. https://doi.org/10.1177/0309133313515293

McLeod T, Samson C, Labrie M et al (2013) Using video acquired from an unmanned aerial vehicle (UAV) to measure fracture orientation in an open-pit mine. Geomatica 67:173–180

Messinger M, Asner G, Silman M (2016) Rapid assessments of amazon forest structure and biomass using small unmanned aerial systems. Remote Sens 8:615. https://doi.org/10.3390/rs8080615

Mossa J, James LA (2013) Impacts of mining on geomorphic systems. In: Treatise on geomorphology, vol. 13. Geomorphology of human disturbances, Climate change, and natural hazards. Academic Press, San Diego, CA, pp 74–95

Neugirg F, Stark M, Kaiser A et al (2016) Erosion processes in calanchi in the Upper Orcia Valley, Southern Tuscany, Italy based on multi-temporal high-resolution terrestrial LiDAR and UAV surveys. Geomorphology 269:8–22. https://doi.org/10.1016/j.geomorph.2016.06.027

Niethammer U, James MR, Rothmund S et al (2012) UAV-based remote sensing of the super-sauze landslide: evaluation and results. Eng Geol 128:2–11. https://doi.org/10.1016/j.enggeo.2011.03.012

Osterkamp WR, Joseph WL (2000) Climatic and hydrologic factors associated with reclamation. In: Barnhisel RI, Darmody RG, Daniels WL (eds) Reclamation of drastically disturbed lands. American Society of Agronomy, Madison, pp 193–215

Passalacqua P, Belmont P, Staley DM et al (2015) Analyzing high resolution topography for advancing the understanding of mass and energy transfer through landscapes: a review. Earth Sci Rev 148:174–193. https://doi.org/10.1016/j.earscirev.2015.05.012

Prosdocimi M, Calligaro S, Sofia G et al (2016) Bank erosion in agricultural drainage networks: new challenges from structure-from-motion photogrammetry for post-event analysis. Earth Surf Process Landf 40:1891–1906. https://doi.org/10.1002/esp.3767

Shahbazi M, Sohn G, Théau J, Ménard P (2015) UAV-based point cloud generation for open-pit mine modelling. Int Arch Photogramm Remote Sens Spat Inf Sci ISPRS Arch 40:313–320. https://doi.org/10.5194/isprsarchives-XL-1-W4-313-2015

Sibson R et al (1981) A brief description of natural neighbour interpolation. Interpret Multivar Data 21:21–36

Sofia G, Marinello F, Tarolli P (2014) A new landscape metric for the identification of terraced sites: the slope local length of auto-correlation (SLLAC). ISPRS J Photogramm Remote Sens 96:123–133. https://doi.org/10.1016/j.isprsjprs.2014.06.018

Sofia G, Bailly J-S, Chehata N et al (2016) Comparison of pleiades and LiDAR digital elevation models for terraces detection in farmlands. IEEE J Sel Top Appl Earth Obs Remote Sens 9:1567–1576. https://doi.org/10.1109/JSTARS.2016.2516900

Sofia G, Masin R, Tarolli P (2017) Prospects for crowd sourced information on the geomorphic "engineering" by the invasive Coypu (*Myocastor coypus*). Earth Surf Process Landf. https://doi.org/10.1002/esp.4081

Stout KJ, Blunt L, Dong WP et al (2000) Development of methods for the characterisation of roughness in three dimensions, 1st edn. Penton Press, Luxembourg

Tarolli P (2014) High-resolution topography for understanding earth surface processes: opportunities and challenges. Geomorphology 216:295–312. https://doi.org/10.1016/j.geomorph.2014.03.008

Tarolli P, Sofia G (2016) Human topographic signatures and derived geomorphic processes across landscapes. Geomorphology 255:140–161. https://doi.org/10.1016/j.geomorph.2015.12.007

Tarolli P, Sofia G, Dalla Fontana G (2012) Geomorphic features extraction from high-resolution topography: landslide crowns and bank erosion. Nat Hazards 61:65–83. https://doi.org/10.1007/s11069-010-9695-2

Tarolli P, Sofia G, Ellis E (2017) Mapping the topographic fingerprints of humanity across earth. Eos (Washington DC). https://doi.org/10.1029/2017EO069637

Tong X, Liu X, Chen P et al (2015) Integration of UAV-based photogrammetry and terrestrial laser scanning for the three-dimensional mapping and monitoring of open-pit mine areas. Remote Sens 7:6635–6662. https://doi.org/10.3390/rs70606635

Townsend PA, Helmers DP, Kingdon CC et al (2009) Changes in the extent of surface mining and reclamation in the central appalachians detected using a 1976–2006 Landsat time series. Remote Sens Environ 113:62–72. https://doi.org/10.1016/j.rse.2008.08.012

Toy TJ, Hadley RF (1987) Geomorphology of disturbed lands. Academic Press, New York

Turner D, Lucieer A, de Jong SM (2015) Time series analysis of landslide dynamics using an unmanned aerial vehicle (UAV). Remote Sens 7:1736–1757. https://doi.org/10.3390/rs70201736

Verhoeven G (2011) Taking computer vision aloft–archaeological three-dimensional reconstructions from aerial photographs with photoscan. Archaeol Prospect 18:67–73

Vidal O, Goffé B, Arndt N et al (2013) Metals for a low-carbon society. Nat Geosci 6:894–896. https://doi.org/10.1038/ngeo1993

Westaway RM, Lane SN, Hicks DM (2000) The development of an automated correction procedure for digital photogrammetry for the study of wide, shallow, gravel-bed rivers. Earth Surf Process Landf 25:209–226

Westoby MJ, Brasington J, Glasser NF et al (2012) "Structure-from-Motion" photogrammetry: a low-cost, effective tool for geoscience applications. Geomorphology 179:300–314. https://doi.org/10.1016/j.geomorph.2012.08.021

Wheaton JM, Brasington J, Darby SE, Sear DA (2010) Accounting for uncertainty in DEMs from repeat topographic surveys: improved sediment budgets. Earth Surf Process Landforms. https://doi.org/10.1002/esp.1886

Wilkinson BH, McElroy BJ (2007) The impact of humans on continental erosion and sedimentation. Geol Soc Am Bull 119:140–156

Woodget AS, Carbonneau PE, Visser F, Maddock IP (2015) Quantifying submerged fluvial topography using hyperspatial resolution UAS imagery and structure from motion photogrammetry. Earth Surf Process Landf 40:47–64. https://doi.org/10.1002/esp.3613

Yucel MA, Turan RY (2016) Areal change detection and 3D modeling of mine lakes using high-resolution unmanned aerial vehicle images. Arab J Sci Eng 41:4867–4878. https://doi.org/10.1007/s13369-016-2182-7

Zhao Y, Feng C, Li D (2014) The major ore clusters of super-large iron deposits in the world, present situation of iron resources in China, and prospect. Acta Geol Sin (English Ed) 88:1895–1915

Affiliations

Jie Xiang[1] · Jianping Chen[1] · Giulia Sofia[2] · Yi Tian[3] · Paolo Tarolli[2]

Jie Xiang
xiangjie@cugb.edu.cn

Giulia Sofia
giulia.sofia@unipd.it

Yi Tian
tianyi@cugb.edu.cn

Paolo Tarolli
paolo.tarolli@unipd.it

[1] School of Earth Sciences and Resources, China University of Geosciences, Beijing 100083, China

[2] Department of Land, Environment, Agriculture and Forestry, University of Padova, Agripolis, viale dell'Università 16, 35020 Legnaro, PD, Italy

[3] School of Land Sciences and Technology, China University of Geosciences, Beijing 100083, China